Coherent order parameter dynamics in SmTe₃

M. Trigo,[1,2,*] P. Giraldo-Gallo,[3,4] M. E. Kozina,[1,2] T. Henighan,[1,2] M. P. Jiang,[1,2] H. Liu,[1,2] J. N. Clark,[1]
M. Chollet,[5] J. M. Glownia,[5] D. Zhu,[5] T. Katayama,[6] D. Leuenberger,[2,3] P. S. Kirchmann,[2]
I. R. Fisher,[2,3] Z. X. Shen,[2,3] and D. A. Reis[1,2,3,7]

[1]*Stanford PULSE Institute, SLAC National Accelerator Laboratory, Menlo Park, California 94025, USA*
[2]*Stanford Institute for Materials and Energy Sciences, SLAC National Accelerator Laboratory, Menlo Park, California 94025, USA*
[3]*Department of Applied Physics, Stanford University, Stanford, California 94305, USA*
[4]*Department of Physics, Universidad de Los Andes, Bogotá 111711, Colombia*
[5]*Linac Coherent Light Source, SLAC National Accelerator Laboratory, Menlo Park, California 94025, USA*
[6]*Japan Synchrotron Radiation Research Institute, 1-1-1 Kouto, Sayo-cho, Sayo-gun, Hyogo 679-5198, Japan*
[7]*Department of Photon Science, Stanford University, Stanford, California 94305, USA*

We present ultrafast optical pump-probe and ultrafast x-ray diffraction measurements of the charge density wave dynamics in SmTe₃ at 300 K. We performed ultrafast x-ray diffraction measurements at the Linac Coherent Light Source to directly probe the dynamics of the finite-wave-vector order parameter. The dynamics reveal coherent oscillations at ∼1.6 THz that become overdamped with increasing fluence. We identify this oscillation with the lattice component of the amplitude mode. Furthermore, our data allow for a clear identification of the amplitude mode frequency in the optical pump-probe data. In both measurements, the system reaches the symmetric phase at high fluence, where the order parameter vanishes and the response (reflectivity and x-ray intensity) is quadratic in the order parameter. This is observed in the x-ray diffraction as a small overdamped modulation near zero intensity. Similar overdamped features are observed in the optical reflectivity at high fluence. A time-dependent Ginzburg-Landau model captures qualitatively the essential features of the experimental observations.

I. INTRODUCTION

Charge density waves (CDWs) [1] are broken-symmetry states of metals that spontaneously develop a valence charge modulation and a gap in the electronic structure concomitant with a frozen lattice distortion with a well-defined wave vector $\mathbf{q}_{cdw}$. The lattice exhibits a Kohn anomaly, a soft phonon mode of the symmetric phase, whose frequency $\omega(\mathbf{q}_{cdw})$ decreases as the transition temperature T_c is approached from above. In the original mechanism proposed by Peierls, the CDW forms due to an electronic instability that occurs because of Fermi-surface nesting between bands separated by $\mathbf{q}_{cdw}$. Later arguments, however, showed that Fermi-surface nesting does not provide predictive power: in most two-dimensional systems the CDW wave vector is not the optimum nesting wave vector, and the wave vector dependence of the electron-phonon matrix elements must be included to obtain the correct ordering wave vector [2].

Over the last few decades we have seen tremendous progress towards materials control at ultrafast timescales using light pulses [3]. With the goal of understanding the materials dynamics, CDWs provide attractive model systems to study the dynamics of order parameters and fluctuations when driven out of equilibrium. In addition, the CDW long-range order typically occurs at a well-defined wave vector, and the

transition can be modeled with a small number of degrees of freedom. Pump-probe methods have the ability to probe the system both near and far from equilibrium as the transition occurs and, from the dynamics, obtain information about the coupling between the participating degrees of freedom. Various ultrafast techniques have been used to probe the transient dynamics of charge density waves: ultrafast x-ray [4–6] and electron [7] diffraction can probe the structural transformation by measuring the intensity of the CDW Bragg peaks, ultrafast optical spectroscopy can probe the spectrum of low-energy excitations and their transient dynamics with excellent frequency resolution [8–10], and time- and angle-resolved photoemission spectroscopy can probe the transient electronic gap and quasiparticle populations [11–13].

The rare-earth tritellurides (RTe₃, with R being a rare-earth ion) have attracted much attention as a model system for studying the interplay between Fermi-surface nesting [14] and electron-phonon coupling [6,15,16] in CDW phenomena. To characterize the effect of electron-phonon coupling, it is important to clearly identify the order parameter and its low-amplitude oscillations, the amplitude mode (AM). Prior ultrafast works have probed this mode indirectly by its modulation of the optical reflectivity [9], Raman scattering [17], photoemission [11–13], and soft-x-ray scattering [6]. Here we present comprehensive ultrafast optical pump-probe and ultrafast x-ray diffraction on SmTe₃ at 300 K that allows us to make a clear assignment of the AM to modulations in the x-ray diffraction signal. SmTe₃ undergoes

*mtrigo@slac.stanford.edu

a CDW transition at $T_c = 416$ K. The high-symmetry phase of SmTe$_3$ crystallizes in the *Cmcm* space group [18] with lattice constants $a = 4.333$, $b = 25.68$, $c = 4.336$ Å. Below T_c the material develops a static CDW [19] with an incommensurate wave vector $\mathbf{q}_{cdw} = (0, 0, q) \approx (0, 0, 2/7)$ (reciprocal-lattice units). The magnitude of the distortion, based on an analysis of the intensity of the CDW sideband relative to the nearest Bragg peak [20], is ~0.04 Å. The sample studied here was a flat single crystal of SmTe$_3$ with dimensions of $4 \times 4 \times 0.3$ mm^3 with the long axis, b, perpendicular to the large sample surface.

Using ultrafast hard x-ray pulses from the Linac Coherent Light Source (LCLS), we measured the dynamics of the lattice component of the order parameter at momentum transfer $\mathbf{Q}_{cdw}$ at varying degrees of photoexcitation. Comparing the pump-probe reflectivity data with the x-ray results allows for the identification of the features observed in reflectivity and separation of the zone-center optical phonons from the relevant mode at $\mathbf{Q}_{cdw}$. We observe that at high fluence the system reaches the symmetric state, where the order parameter vanishes. Moreover, the order parameter oscillates around zero, which is manifested in diffraction as an oscillation of the intensity of the nearly suppressed CDW Bragg peaks. A time-dependent Ginzburg-Landau model explains qualitatively the dynamics of the lattice order over the range of fluences measured.

We have organized the paper as follows: we first present a phenomenological model of the dynamics of the order parameter based on the time-dependent Ginzburg-Landau (GL) equation. In this section we also establish the nomenclature used in the rest of the paper and derive phenomenological expressions for the dielectric constant and x-ray intensity for small perturbations of the order parameter. Following the model, we introduce the ultrafast x-ray diffraction results and analyze these in the framework of the GL model. Then we present the optical pump-probe results and compare them with the x-ray data. The concluding paragraph summarizes the findings.

II. GENERAL FRAMEWORK

Here we develop a general model that describes phenomenologically the dynamics of the lattice, including the anharmonic regime at high fluence and its effect on the x-ray structure factor and the optical response. We model the average lattice distortion of the CDW using a time-dependent extension of the Ginzburg-Landau (TDGL) formalism for second-order phase transitions [5,10]. The model assumes that the dynamics of the transition can be described by a real order parameter, the amplitude of the lattice distortion at $\mathbf{q}_{cdw}$, and ignores phase fluctuations at these timescales [10]. The potential is

$$V(x) = \tfrac{1}{2} a(\eta - 1)x^2 + \tfrac{1}{4} bx^4, \quad (1)$$

where $a > 0$ and $b > 0$. Here $\eta \geqslant 0$ acts as a control parameter that in equilibrium has the form $\eta = T/T_c$. For $\eta = 0$ the system is in a double-well configuration with two minima at $x = \pm x_0 = \pm\sqrt{a/b}$. Defining the normalized order parameter $y = x/x_0$, $y = 1$ corresponds to the equilibrium ordered phase, and $y = 0$ corresponds to the high-symmetry phase, as shown
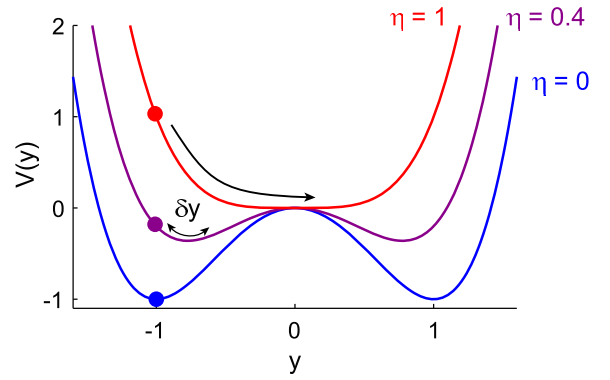

FIG. 1. Normalized Ginzburg-Landau potential $V(y)$ of the anharmonic lattice dynamics model for various levels of excitation.

schematically in Fig. 1. In terms of y, Eq. (1) reads

$$V(y) = \frac{ax_0^2}{4}[2(\eta - 1)y^2 + y^4]. \quad (2)$$

The equation of motion for y is

$$\frac{1}{a}\ddot{y} + [\eta(t) - 1]y + y^3 + \frac{2\Gamma}{a}\dot{y} = 0, \quad (3)$$

with initial conditions $y(0) = 1$, $\dot{y}(0) = 0$, which corresponds to the system in the ordered phase at $t < 0$. The last term in (3) accounts for damping of the dynamics. We describe the photoexcitation by introducing a time-dependent $\eta = \eta(t) = e^{-\beta t}\Theta(t)$, with $\Theta(t)$ being a unit step function. As we show in detail below, in the low-fluence limit, Eq. (3) reduces to the displacive excitation of coherent phonons (DECP) model of Ref. [21], where $-\eta/2$ becomes the shifted equilibrium position of the potential. To account for the experimental observations, the relaxation rate of the photoexcited potential β is assumed to be fluence dependent and is allowed to vary when fitting the model.

A. X-ray structure factor

The x-ray structure factor for the CDW sideband was derived by Overhauser [20]. To first order in the CDW distortion $\mathbf{x}$, the intensity at momentum transfer $\mathbf{Q}_{cdw} = \mathbf{q}_{cdw} + \mathbf{K}$ near reciprocal-lattice vector $\mathbf{K}$ is [20]

$$I(\mathbf{Q}_{cdw}) = J_1^2(\mathbf{Q} \cdot \mathbf{x}) \approx \tfrac{1}{4}[\cos(\alpha)Qx_0y]^2, \quad (4)$$

where J_1 is a Bessel function of the first kind, $Q = ||\mathbf{Q}||$, and α is the angle between $\mathbf{Q}$ and $\mathbf{x}$. As expected, Eq. (4) respects the inversion symmetry $y \to -y$ of the disordered phase. It is convenient to normalize the intensity to $I(t < 0)$, which simplifies to

$$\tilde{I} = \frac{I(\mathbf{Q}_{cdw}, t)}{I(\mathbf{Q}_{cdw}, t < 0)} = \frac{y^2(t)}{y^2(t < 0)} = y^2(t) \quad (5)$$

since $y(t < 0) = 1$. When comparing the model with time-resolved diffraction results, we will refer to $\tilde{I}$ unless otherwise stated.

B. Dielectric constant

As developed in Ref. [22], the expansion of the dielectric constant of a system near a second-order phase transition in

terms of the order parameter y is [22]

$$\epsilon \approx \epsilon_0 + d\, y^2, \qquad (6)$$

where $d = \partial^2 \epsilon / \partial y^2$. Here again the first term in the expansion allowed by symmetry is quadratic in y.

C. Small-amplitude limit and relation to DECP

In the low-fluence regime, $\eta \ll 1$, the system stays near the ordered phase, $y = 1$, and we can approximate $y \approx 1 + \delta y$, with $\delta y \ll 1$. Expanding the equation of motion (3) to first order in δy and η, we get

$$\delta\ddot{y} + \Omega^2 \left(\delta y + \frac{\eta(t)}{2} \right) + 2\Gamma \delta\dot{y} = 0, \qquad (7)$$

where $\Omega = \sqrt{2a}$. As expected, this is the equation of motion for the DECP model (Eq. (3) in [21]) with a shifted equilibrium position $Q_0(t) = -\eta(t)/2$. Note that the curvature of the potential is unchanged to first order in δy and η.

In the limit $\delta y \ll 1$, the quadratic equations for the x-ray intensity (4) and dielectric constant (6) become

$$I \approx \tfrac{1}{4} [\cos(\alpha) Q x_0]^2 \left(1 - \tfrac{1}{2} \delta y \right) \qquad (8)$$

and

$$\epsilon \approx \epsilon_0 + d \left(1 - \tfrac{1}{2} \delta y \right), \qquad (9)$$

respectively. We note that δy is the displacement of the so-called *amplitude mode* of the CDW, and the linear dependence of ϵ on δy makes the AM Raman active in the ordered phase [23]. For the same reason, the linear dependence of these quantities on δy means that a coherent motion of δy appears as a modulation of $\tilde{I}$ or ϵ as $\sim \cos(\Omega t)$.

For completeness, the solution to Eq. (7) is [21]

$$\delta y(t) = A \left\{ e^{-\beta t} - e^{-\Gamma t} \left(\cos \Omega t - \frac{\beta - \Gamma}{\Omega} \sin \Omega t \right) \right\} \Theta(t), \qquad (10)$$

with

$$A = -\frac{\eta(0)}{2} \frac{\Omega^2}{\beta^2 + \Omega^2 - 2\Gamma\beta}. \qquad (11)$$

Here the first term in Eq. (10) corresponds to the inhomogeneous solution with the source term $\eta(t)$ that shifts the equilibrium position, and the second term comes from the homogeneous, oscillatory solution. For $\Gamma/\Omega \ll 1$ the amplitude A reduces to

$$A = -\frac{\eta(0)}{2}. \qquad (12)$$

As expected, the parameters of the DECP model are directly related to those of the anharmonic equation of motion, Eq. (3), in the limit $\delta y \ll 1$, $\eta \ll 1$.

III. ULTRAFAST X-RAY DIFFRACTION

The ultrafast diffraction experiment was carried out at the x-ray pump probe (XPP) instrument at the LCLS [24] with x-ray pulses <50 fs in duration at a photon energy of 9.5 keV

selected using a diamond double-crystal monochromator that provides 0.5 eV bandwidth. The x-ray probe was focused to 0.02×0.1 mm². The pump consisted of 50-fs pulses from a regenerative Ti:sapphire amplifier centered at 800 nm focused to a cross-sectional area of 0.05×0.2 mm². The pump polarization was perpendicular to the sample surface (p polarization). An area detector (Cornell-SLAC pixel array detector) was positioned at ~1 m from the sample and was rotated to capture the various Bragg reflections. To match the optical (~20 nm) and x-ray penetration depths we implemented a grazing incidence geometry. The incidence x-ray angle of $0.3°$ was accurately calibrated by measuring the deflection by x-ray total external reflection at small angles. The arrival time of each optical-pump, x-ray-probe sequence was measured on every shot, and the pump-probe delay was corrected in postprocessing, yielding a time resolution of <80 fs.

In Figs. 2(a)–2(c) we show the dynamics of $\tilde{I}$ of three different CDW diffraction peaks for various incident fluences. The intensity is integrated over the entire diffraction peak and normalized by the intensity without the pump $I_0(\mathbf{Q}_{cdw})$. For clarity in what follows we drop the $(\mathbf{Q}_{cdw})$ argument. The low-fluence traces (top trace in each panel) show a 20% decrease in $\tilde{I}$ and clear oscillations with frequency (period) of ~1.55 THz (650 fs) that decay within a few picoseconds. Based on the estimated static distortion $x_0 \sim 0.04$ Å [25], the amplitude of the motion corresponding to the lowest-fluence trace is $|x_0 \delta y| \sim 8 \times 10^{-3}$ Å. All the traces are shifted horizontally by the same amount to the $t = 0$ time obtained by the fitting procedure described below. Momentum conservation ensures that to leading order, only phonon modes with wave vector $\mathbf{q}_{cdw}$ contribute to $\tilde{I}$. Thus, x-ray scattering at the CDW wave vector avoids the contribution from other Raman-active phonon modes at the zone center [9,13] and isolates the lattice distortion of the AM. Thus, we ascribe these oscillations to the displacement of the amplitude mode δy, which modulates the intensity at $\mathbf{Q}_{cdw}$ through Eq. (8). The green dashed traces in Figs. 2(a)–2(c) correspond to a fit of the low-amplitude solution [Eq. (10)] to the lowest-fluence trace with $\Omega/2\pi = 1.55$ THz, $A = 0.085$, $\Gamma = 1.8$ THz, and $\beta = 0.65$ THz (also listed in Table I).

TABLE I. Parameters of the TDGL fit and DECP fits of Eq. (10). The errors in the TDGL fits were estimated by running 2000 independent fits with multiple random initial conditions (within 20% of the best solution); the values reported correspond to the standard deviation from those fits whose residue is within 10% of the best fit. The errors in the DECP are 95% confidence intervals. Note that $\Omega = \sqrt{2a}$, but we report Ω for the TDGL fits for easier comparison with DECP.

F (mJ/cm²)	$\Omega/(2\pi)$ (THz)	$\eta(0)$ (arbitrary units)	Γ (THz)	β (THz)
0.1	1.60(2)	0.163(3)	1.89(7)	0.61(18)
0.25	1.6[a]	0.47(1)	3.13(15)	0.142(2)
0.5	1.6[a]	0.890(1)	4.53(6)	6.7×10^{-3} [b]
1	1.6[a]	2.0(1)	2.97(7)	10^{-5} [b]
0.1 (DECP)	1.55(9)	0.17(3)	1.8(4)	0.65(8)

[a] Value was fixed at the result of the fit for 0.1 mJ/cm².

[b] Value was not possible to fit due to the short measurement window and was kept fixed.

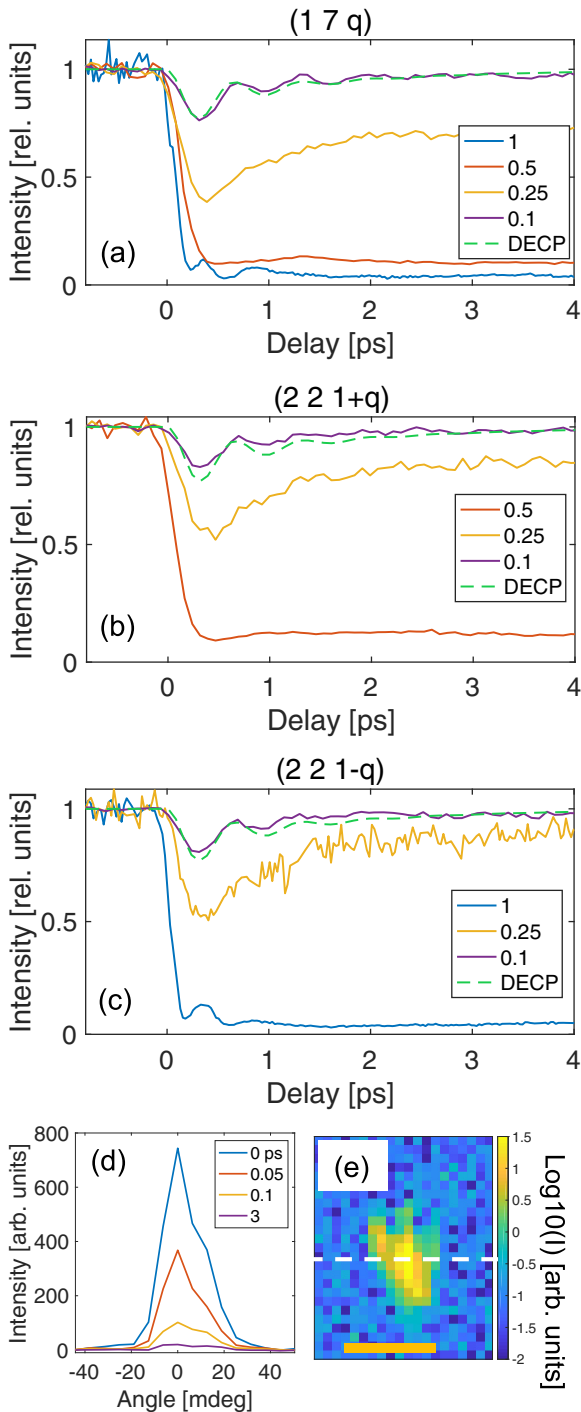FIG. 2. Dynamics of CDW x-ray diffraction $\tilde{I}$ for several incident fluences for CDW peaks (a) $(1\,7\,q)$, (b) $(2\,2\,1+q)$, and (c) $(2\,2\,1-q)$. The legend in (a)–(c) indicates the incident fluence (in mJ/cm²). The green dashed line is a fit using Eq. (10); the parameters of the fit (given in the text) are the same for all panels. (d) Line-out of the intensity across the detector along the dashed line indicated in (e) for representative delays. (e) The detector image of the $(1\,7\,q)$ CDW Bragg peak; the horizontal scale bar is $9 \times 10^{-4}\,\text{Å}^{-1}$, and the intensity scale is logarithmic.

As the fluence increases, we observe a strong suppression in $\tilde{I}$ as well as a nearly complete softening of the oscillations at fluences ∼0.25–0.5 mJ/cm². At the maximum

fluence of 1 mJ/cm², $\tilde{I} \approx 0$, and we observe two overdamped oscillations near delay $t \sim 0.5$ ps [see, e.g., 1 mJ/cm² traces in Figs. 2(a) and 2(c)]. This can be understood qualitatively as the order parameter crossing to the opposite side of the quartic potential well, indicated by the arrow on the top curve in Fig. 1. At high excitation densities, δy becomes large (i.e., y can deviate significantly from $y = 1$), and one must consider Eq. (4) instead of (8) to properly describe the x-ray intensity. Also, because of this quadratic dependence, the period of the oscillation observed in the 1 mJ/cm² traces is half of the period of oscillation of $y(t)$ around $y = 0$ in the new potential (top trace in Fig. 1), as has been previously observed in $K_{0.3}MoO_3$ [5]. A similar crossover from Eqs. (9) to (6) as the symmetric phase is approached is also observed in the pump-probe reflectivity presented below. We will discuss the observed fluence dependence scaling (seen clearly in the inset of Fig. 6 below) in more detail later in the context of the TDGL model.

IV. ULTRAFAST OPTICAL REFLECTIVITY

As we see next, many of the features of the order parameter dynamics pointed out above are also visible in an ultrafast reflectivity probe. We present here an optical-pump, optical-probe reflectivity measurement of $SmTe_3$ for similar excitation fluences. The transient reflectivity at 800 nm was measured with 45-fs pulses from a Coherent RegA laser system at a repetition rate of 250 kHz. The pump and probe were near collinear at normal incidence, and the pump was chopped at 2 kHz. The reflected beam intensity was collected with a photodiode, and the signal at the chopper frequency was measured with a lock-in amplifier. The pump and probe beam sizes (full width at half maximum) at the sample position were 60 and 25 μm, respectively.

Figure 3(a) shows the time-domain reflectivity of $SmTe_3$ at 300 K for increasing incident fluence, indicated in the legend (in mJ/cm²). These data have more oscillatory components than the x-ray traces in Fig. 2 because the reflectivity is modulated, in principle, by all possible Raman-active modes in the material consistent with selection rules. Figure 3(b) shows a zoomed-in view at early times of the same data in Fig. 3(a) but normalized by the respective fluence to highlight the features at low fluence. The dashed line in Fig. 3(b) shows a fit of Eq. (10) to the 0.033 mJ/cm² trace, whose frequency most closely matches that of the 0.1 mJ/cm² x-ray data in Fig. 2. For low fluence the time-domain trace shows several oscillations corresponding to various Raman-active phonons, including the AM, which is folded back to zone center in the distorted phase [9,17], a consequence of the static distortion in Eq. (9). The AM softens with increasing fluence and becomes overdamped as fluence reaches $F \sim 0.33$ mJ/cm². This is made clear when normalizing the time traces by the incidence fluence [Fig. 3(b)] and is observed as a delay of the first maximum of oscillation. For $F \sim 0.7$ mJ/cm² [top trace in Fig. 3(a)] we observe a fast, single-cycle oscillation, whose period is shorter than that of the low-fluence AM and which resembles the high-fluence trace in the x-ray structure factor [compare with the high-fluence traces in Figs. 2(a) and 2(c)]. At this fluence the system can reach $y \approx 0$ (see the discussion of Fig. 4 for a comparison between the fluences in the x-ray and optical experiments). Thus, as before, at this
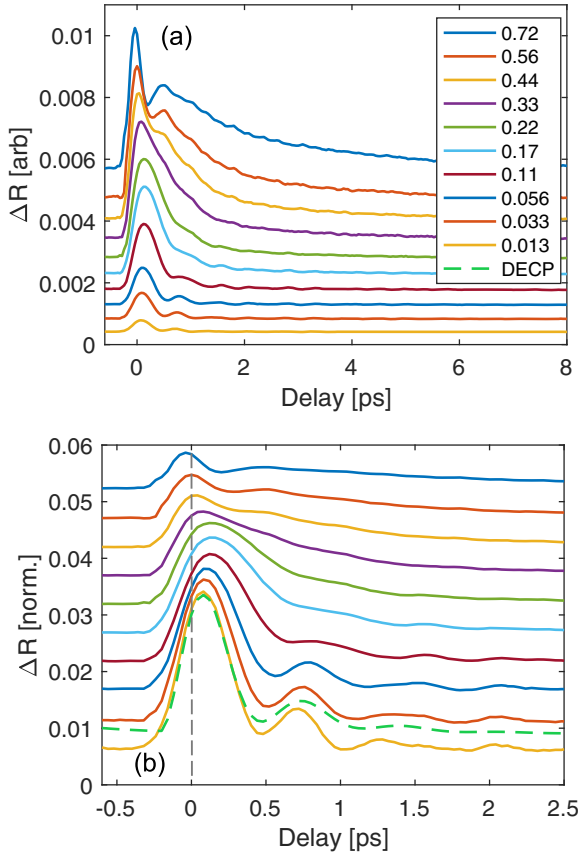
FIG. 3. (a) Differential reflectivity at a wavelength of 800 nm as a function of pump-probe delay. The pump wavelength is 800 nm, and the incident fluence for each trace is labeled in the legend in (mJ/cm^2). (b) Zoomed-in view of the data in (a) normalized by the incident fluence. The dashed curve is a DECP fit of 0.033 mJ/cm^2 with $\Omega/2\pi = 1.55$ THz, $\gamma = 2.5$ THz, $\beta = 1.95$ THz. The vertical dashed line marks the $t = 0$ point.

excitation level we expect a crossover between Eqs. (9) and (6). Interestingly, a consequence of Eq. (6) is that in the region near $y = 0$, the lattice motion is not probed through first-order Raman as in the case of δy, but the deviations of the order parameter from $y = 0$ couple with the probe as a second-order Raman process [10,23,26].
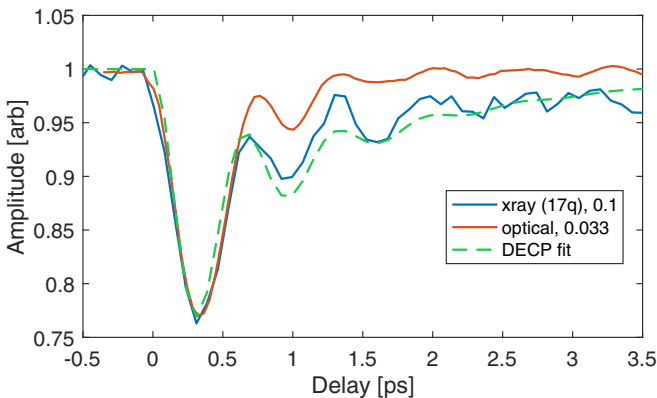

FIG. 4. Comparison between x-ray and optical data for the lowest fluence. The dashed line is the DECP fit of the x-ray data in Fig. 2.
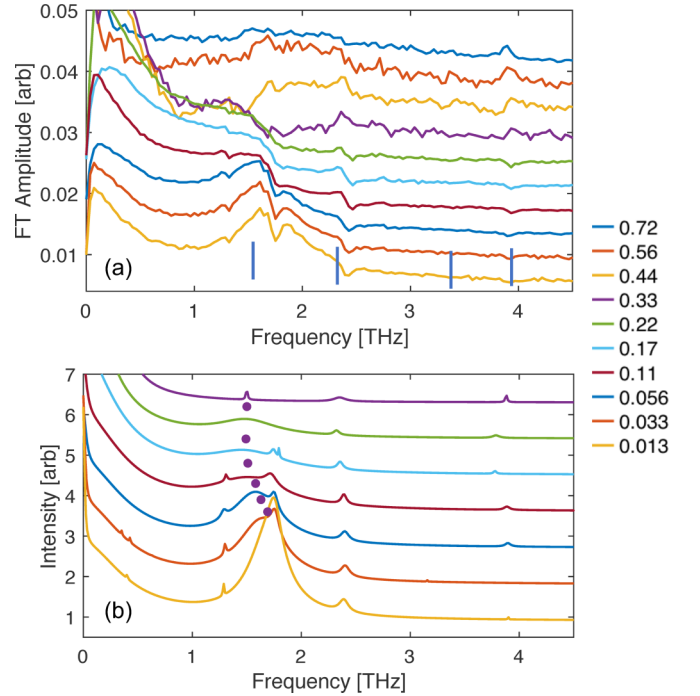

FIG. 5. Frequency spectrum of the optical reflectivity data in Fig. 3 extracted from (a) a Fourier transform (FT) after background subtraction and (b) the linear prediction procedure discussed in the text [27]. The incident fluence for each trace is indicated next to the FT traces (in mJ/cm^2). The purple dots in (b) mark the frequency of the LP component ascribed to the soft mode. Vertical bars indicate the frequencies of the most prominent phonon modes of SmTe₃ observed in Raman scattering [17].

For comparison between x-ray and optical results we plot in Fig. 4 the two traces of low-fluence x-ray and optical data that most closely match (the optical data have been inverted and scaled to match the overall amplitude). The dashed line here is the DECP fit from Fig. 2(a). We observe that the oscillations in the 0.033 mJ/cm^2 optical reflectivity curve best match the low-fluence oscillations in the x-ray data (0.1 mJ/cm^2), which provides a robust comparison between the fluences of the two measurements and removes systematic errors when comparing excitation levels between them. This comparison suggests that the soft-mode component in the optical data is related to the lattice component of the order parameter at $\mathbf{q}_{\mathrm{cdw}}$.

Figure 5(a) shows the Fourier transform of the data in Fig. 3 after subtraction of a double exponential that represents the nonoscillatory contribution from photoexcited quasiparticles [8,10]. It is clear from Fig. 5(a) that there are several modes in the data with a broad double feature at ~1.65 THz and two clear modes at 2.5 and 3.95 THz. The most prominent broad feature at ~1.65 THz softens as a function of fluence, while the frequencies of the other modes remain static as fluence increases. The vertical bars indicate the frequencies of the most prominent Raman-active modes of SmTe₃ observed in [17].

As an alternative approach to obtain the frequency content of these oscillations, we treat the data using a linear prediction algorithm. This algorithm operates on the time-domain data

and assumes that the signal is a superposition of an unknown number of decaying cosines, some of which may have zero frequency (i.e., pure decaying exponentials). Since it does not involve a least-squares fit of a function to the data, this method is a direct and more robust way of extracting the parameters of exponentially decaying cosines. Furthermore, the number of oscillators is determined from the statistical properties of the data [27,28]. Following Ref. [27], the procedure relies on linear prediction of each observation r_n in terms of M previous ones: $r_n = a_1 r_{n-1} + a_2 r_{n-2} + \cdots + a_M r_{n-M}$ for $n = M + 1, \ldots, N$, where N is the number of time points equally spaced by Δt. This overdetermined linear set of equations can be solved for the coefficients a_n. A subset of $2K < M$ of these coefficients, where K is the number of oscillators in the data, becomes the coefficients of a polynomial whose complex roots $z_i = \exp[(-b_i \pm i\omega_i)\Delta t]$ contain the frequency ω_i and damping b_i of each oscillator. As described in [27] the procedure outputs the frequencies, decay constants, amplitudes, and phases of the oscillators and can include pure decaying exponential (zero-frequency) components. For presentation purposes we compute the total spectrum as a sum of Lorentzian functions

$$I(\omega) = \sum_j A_j \frac{b}{(\omega - \omega_j)^2 + b^2},$$

where the amplitudes A_j, frequencies ω_j, and dampings b_j are extracted from this linear prediction algorithm.

Figure 5(b) shows the spectrum of the low-fluence traces obtained by applying linear prediction to the time-domain traces in Fig. 3(a). The frequency of the soft mode obtained with this method is indicated by the dot ∼1.6 THz above the corresponding trace. Note that not only does the frequency decrease but the width of this soft-mode component increases with increasing fluence, consistent with the observations in the FT [Fig. 5(a)]. We point out that the AM, whose frequency is ∼2.2 THz near 10 K [9], softens strongly as temperature increases towards the critical temperature T_c and crosses other phonon modes near 1.75 THz at 100 K below T_c [9]. Extrapolation from the literature observation for HoTe$_3$, DyTe$_3$, and TbTe$_3$ [9] to SmTe$_3$ indicates that the AM crosses the 1.75-THz mode around $T \sim 280$ K. Thus, the AM at 300 K is already significantly softened, and photoexcitation likely contributes additional softening. We further note that the 2.5-THz mode does not soften and remains visible even for fluences >0.25 mJ/cm^2, where the CDW diffraction is strongly suppressed. Taking into consideration the x-ray and optical comparison in Fig. 4, we identify the soft mode at 1.6 THz with the 1.55-THz oscillations in the low-fluence x-ray traces in Fig. 2 and assign it to the AM. Note that time- and angle-resolved photoemission spectroscopy shows modes at 2.2 and 2.5 THz at relatively low fluence [13], and per the discussion above, we associate the softened 1.6-THz mode observed here with the 2.2-THz mode seen in Ref. [13].

V. HIGH-FLUENCE REGIME

We now turn our attention to the high-fluence x-ray data. As the incident fluence F increases, we observe a suppression of the oscillatory dynamics for fluences above 0.25 mJ/cm^2 and almost complete extinction of the CDW intensity at
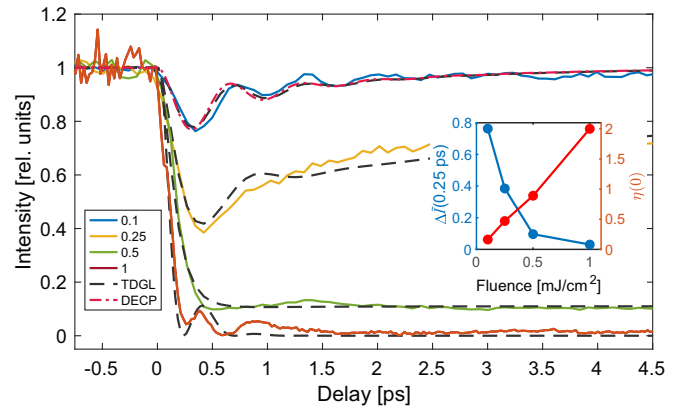

FIG. 6. Time-dependent Ginzburg-Landau model of the dynamics of the order parameter. The solid lines are the time dependence of the structure factor for the (17q) reflection as in Fig. 2(a). The dark dashed lines are the solutions to the TDGL for the values reported in Table I. For comparison, the dash-dotted line shows the DECP fit from Fig. 2. The inset shows the fluence dependence of the measured intensity $\tilde{I}(0.25\,\text{ps})$ and the fitted value of $\eta(0)$ (from Table I).

$F > 0.5$ mJ/cm^2 (Fig. 2). We note that the Bragg peak width (inverse of the correlation length) does not appreciably change over the range of delays probed here, as seen in the Bragg peak cross sections in Fig. 2(e) and consistent with previous resonant diffraction measurements [6]. This suggests that, unlike the thermal transition [19] where the correlation length diverges, the ultrafast destruction of the CDW order proceeds without the creation of topological defects [29] at these timescales.

Figure 6 shows the fit of the numerical integration of Eq. (3) (black dashed lines) together with the experimental data for the (17q) Bragg peak from Fig. 2(a) for various fluences (solid lines). The frequency was varied only when fitting the 0.1 mJ/cm^2 data and was kept fixed at the resulting value when fitting the other fluences. The fit parameters are given in Table I. As can be seen in Fig. 6, this model reproduces the dynamics of the structure factor for the entire delay and fluence ranges. In the limit of low fluence, $y \approx 1 + \delta y$, and $\delta y(t)$ reduces to the DECP solution from Eq. (10), which is shown by the dash-dotted line in Fig. 6. At this fluence the model predicts a ∼20% suppression of the intensity together with time-dependent oscillations due to the low-amplitude vibrations of δy as observed experimentally in the top trace of Fig. 6. Experimentally, we observe that the intensity at $t = 0.25$ ps, $\tilde{I}(0.25\,\text{ps})$, sharply decreases with fluence, as can be seen in the inset of Fig. 6. This fluence scaling in the inset of Fig. 6 is a consequence of the ∼y^2 form of Eq. (4). As fluence increases, the motion in $y(t)$ becomes overdamped at $F = 0.25$ mJ/cm^2 (which corresponds to $\eta = 0.5$; see Table I). The critical point $\eta = 1$ is reached for $F \sim 0.5$ mJ/cm^2, which achieves nearly complete suppression of the CDW Bragg peak. Note that while $\tilde{I}(0.25\,\text{ps})$ scales as y^2, the scaling of $\eta(0)$ with fluence is linear (see inset in Fig. 6, from Table I). At 1 mJ/cm^2, $\eta = 2$, and the system is pushed well into the high-symmetry phase, where the potential has a single minimum at $y = 0$ (top trace in Fig. 1); after the sudden excitation the order parameter crosses the $y = 0$ point and

performs two overdamped oscillations before fully decaying, as seen in Figs. 2(a) and 2(c). A similar crossover behavior is observed in the reflectivity data in Fig. 3 for comparable fluences ($F > 0.5$ in Fig. 3). The TDGL model described above provides a phenomenological description of these observations and qualitatively explains the behavior of both the x-ray and reflectivity data over the entire regime of fluences.

VI. CONCLUSIONS

In conclusion, we have presented a comprehensive ultrafast x-ray and optical study of the lattice dynamics of SmTe₃. We used x-ray diffraction to directly probe the dynamics of order parameter at $\mathbf{q}_{\mathrm{cdw}}$, which was previously accessed only indirectly. Comparison of ultrafast reflectivity measurements with the x-ray results allows for unequivocal identification of the amplitude mode in the optical pump probe. In the high-excitation regime, the lattice distortion reaches the symmetric structure at $y = 0$ and can overshoot for even higher fluence excitation. The overshoot and subsequent modulation of the order parameter around $y = 0$ appear as overdamped oscillations slightly above $\tilde{I} = 0$. Similar oscillatory features are observed in reflectivity for high excitation levels. Finally, a phenomenological time-dependent Ginzburg-Landau model describes qualitatively the large-amplitude dynamics of the lattice distortion.

[1] G. Grüner, Rev. Mod. Phys. **60**, 1129 (1988).

[2] M. D. Johannes and I. I. Mazin, Phys. Rev. B **77**, 165135 (2008).

[3] D. N. Basov, R. D. Averitt, and D. Hsieh, Nat. Mater. **16**, 1077 (2017).

[4] E. Möhr-Vorobeva, S. L. Johnson, P. Beaud, U. Staub, R. De Souza, C. Milne, G. Ingold, J. Demsar, H. Schaefer, and A. Titov, Phys. Rev. Lett. **107**, 036403 (2011).

[5] T. Huber, S. O. Mariager, A. Ferrer, H. Schäfer, J. A. Johnson, S. Grübel, A. Lübcke, L. Huber, T. Kubacka, C. Dornes, C. Laulhe, S. Ravy, G. Ingold, P. Beaud, J. Demsar, and S. L. Johnson, Phys. Rev. Lett. **113**, 026401 (2014).

[6] R. G. Moore, W. S. Lee, P. S. Kirchman, Y. D. Chuang, A. F. Kemper, M. Trigo, L. Patthey, D. H. Lu, O. Krupin, M. Yi, D. A. Reis, D. Doering, P. Denes, W. F. Schlotter, J. J. Turner, G. Hays, P. Hering, T. Benson, J.-H. Chu, T. P. Devereaux, I. R. Fisher, Z. Hussain, and Z.-X. Shen, Phys. Rev. B **93**, 024304 (2016).

[7] M. Eichberger, H. Schäfer, M. Krumova, M. Beyer, J. Demsar, H. Berger, G. Moriena, G. Sciaini, and R. J. D. Miller, Nature (London) **468**, 799 (2010).

[8] J. Demsar, K. Biljaković, and D. Mihailovic, Phys. Rev. Lett. **83**, 800 (1999).

[9] R. V. Yusupov, T. Mertelj, J.-H. Chu, I. R. Fisher, and D. Mihailovic, Phys. Rev. Lett. **101**, 246402 (2008).

[10] R. Yusupov, T. Mertelj, V. V. Kabanov, S. Brazovskii, P. Kusar, J.-H. Chu, I. R. Fisher, and D. Mihailovic, Nat. Phys. **6**, 681 (2010).

[11] F. Schmitt, P. S. Kirchmann, U. Bovensiepen, R. G. Moore, J.-H. Chu, D. H. Lu, L. Rettig, M. Wolf, I. R. Fisher, and Z.-X. Shen, New J. Phys. **13**, 063022 (2011).

[12] L. Rettig, J.-H. Chu, I. R. Fisher, U. Bovensiepen, and M. Wolf, Faraday Discuss. **171**, 299 (2014).

[13] D. Leuenberger, J. A. Sobota, S.-L. Yang, A. F. Kemper, P. Giraldo-Gallo, R. G. Moore, I. R. Fisher, P. S. Kirchmann, T. P. Devereaux, and Z.-X. Shen, Phys. Rev. B **91**, 201106 (2015).

[14] V. Brouet, W. L. Yang, X. J. Zhou, Z. Hussain, N. Ru, K. Y. Shin, I. R. Fisher, and Z. X. Shen, Phys. Rev. Lett. **93**, 126405 (2004).

[15] H.-M. Eiter, M. Lavagnini, R. Hackl, E. A. Nowadnick, A. F. Kemper, T. P. Devereaux, J.-H. Chu, J. G. Analytis, I. R. Fisher, and L. Degiorgi, Proc. Natl. Acad. Sci. USA **110**, 64 (2013).

[16] M. Maschek, S. Rosenkranz, R. Heid, A. H. Said, P. Giraldo-Gallo, I. R. Fisher, and F. Weber, Phys. Rev. B **91**, 235146 (2015).

[17] M. Lavagnini, A. Baldini, A. Sacchetti, D. Di Castro, B. Delley, R. Monnier, J.-H. Chu, N. Ru, I. R. Fisher, P. Postorino, and L. Degiorgi, Phys. Rev. B **78**, 201101 (2008).

[18] B. K. Norling and H. Steinfink, Inorg. Chem. **5**, 1488 (1966).

[19] N. Ru, C. L. Condron, G. Y. Margulis, K. Y. Shin, J. Laverock, S. B. Dugdale, M. F. Toney, and I. R. Fisher, Phys. Rev. B **77**, 035114 (2008).

[20] A. W. Overhauser, Phys. Rev. B **3**, 3173 (1971).

[21] H. J. Zeiger, J. Vidal, T. K. Cheng, E. P. Ippen, G. Dresselhaus, and M. S. Dresselhaus, Phys. Rev. B **45**, 768 (1992).

[22] V. L. Ginzburg, Sov. Phys. Usp. **5**, 649 (1963).

[23] V. Ginzburg, A. Levanyuk, and A. Sobyanin, Phys. Rep. **57**, 151 (1980).

[24] M. Chollet, R. Alonso-Mori, M. Cammarata, D. Damiani, J. Defever, J. T. Delor, Y. Feng, J. M. Glownia, J. B. Langton, S. Nelson, K. Ramsey, A. Robert, M. Sikorski, S. Song, D. Stefanescu, V. Srinivasan, D. Zhu, H. T. Lemke, and D. M. Fritz, J. Synchrotron Radiat. **22**, 503 (2015).

[25] An estimate can be obtained from the ratio of the CDW intensity to that of the nearest Bragg peak: $I(17q)/I(170) \sim (\mathbf{Q} \cdot \mathbf{x})^2$ [20].

[26] T. Henighan, M. Trigo, M. Chollet, J. N. Clark, S. Fahy, J. M. Glownia, M. P. Jiang, M. Kozina, H. Liu, S. Song, D. Zhu, and D. A. Reis, Phys. Rev. B **94**, 020302 (2016).

[27] H. Barkhuijsen, R. de Beer, W. Bovée, and D. van Ormondt, J. Magn. Reson. **61**, 465 (1985).

[28] F. Wise, M. Rosker, G. Millhauser, and C. Tang, IEEE J. Quantum Electron. **23**, 1116 (1987).

[29] W. S. Lee, Y. D. Chuang, R. G. Moore, Y. Zhu, L. Patthey, M. Trigo, D. H. Lu, P. S. Kirchmann, O. Krupin, M. Yi, M. Langner, N. Huse, J. S. Robinson, Y. Chen, S. Y. Zhou, G. Coslovich, B. Huber, D. A. Reis, R. A. Kaindl, R. W. Schoenlein, D. Doering, P. Denes, W. F. Schlotter, J. J. Turner, S. L. Johnson, M. Först, T. Sasagawa, Y. F. Kung, A. P. Sorini, A. F. Kemper, B. Moritz, T. P. Devereaux, D. H. Lee, Z. X. Shen, and Z. Hussain, Nat. Commun. **3**, 838 (2012).